inorganics

MDPI

Article

Peppermint-Mediated Green Synthesis of Nano ZrO_2 and Its Adsorptive Removal of Cobalt from Water

Ibrahem Mohamed Abouzeid Hasan *, Hanan Salah El-Din and Ahmed A. AbdElRaady

Chemistry Department, Faculty of Science, South Valley University, Qena 83523, Egypt
* Correspondence: hasan111167@gmail.com; Tel.: +20-1006-753-052

Abstract: Zirconium oxide nanoparticles (ZrO_2NPs) were green synthesized for the first time using an aqueous peppermint extract as a precipitating and capping agent. Addition of the extract to Zr^{4+} solution was followed by calcination of the resulting precipitate at 570 and 700 °C to form ZrO_2NPs570 and ZrO_2NPs700, respectively. These oxides were characterized using X-ray diffraction, transmission electron microscopy, and BET surface area analysis, and used as adsorbents for cobalt ions (Co^{2+}) in water. The effects of pH, initial Co^{2+} concentration, ZrO_2NPs mass, and contact time on adsorption efficiency were studied. Characterization results showed formation of cubic ZrO_2 with average crystallite sizes (XRD data) of 6.27 and 7.26 nm for ZrO_2NPs570 and ZrO_2NPs700, respectively. TEM images of the two oxides exhibited nearly spherical nanoparticles and BET surface area measurements indicated the formation of mesoporous oxides having surface areas of 94.8 and 62.4 m^2/g, respectively. The results of the adsorption study confirmed that the synthesized ZrO_2NPs can be efficiently used for the adsorption of Co^{2+} from water. The uptake of Co^{2+} from the treated solution is favored at pH values higher than its point of zero charge (6.0). In addition, the adsorption of Co^{2+} by ZrO_2 follows a pseudo-second order kinetics (R^2 = 1.0) and can be explained by the Langmuir adsorption isotherm (R^2 = 0.973).

Keywords: adsorption; cobalt ions; peppermint; synthesis; ZrO_2NPs

check for updates

Citation: Hasan, I.M.A.; Salah El-Din, H.; AbdElRaady, A.A. Peppermint-Mediated Green Synthesis of Nano ZrO_2 and Its Adsorptive Removal of Cobalt from Water. *Inorganics* **2022**, *10*, 257. https://doi.org/10.3390/inorganics10120257

Academic Editor: Carlos Martínez-Boubeta

Received: 22 October 2022
Accepted: 28 November 2022
Published: 12 December 2022

1. Introduction

Zirconium oxide (ZrO_2) is a wide direct band gap semiconductor and considered a multifunctional material due to its unique physical and chemical properties, such as high thermal stability, excellent mechanical characteristics, non-toxicity, and adsorption ability. It was used in many scientific and technological fields, such as catalysis, adsorption, biology, optics, electronics, magnetism, and dental medicine [1–8].

Adsorption is a well-known technique for removing various organic and inorganic contaminants from aqueous media [9,10]; as a surface phenomenon, it involves the formation of physical or chemical bonds between the adsorbate molecules and the adsorbent surface. Accordingly, adsorbent surface properties such as morphology, surface area, pore size distribution, charge, nature of active sites, and their distribution and density determine their efficiency. These properties are greatly influenced by preparation method and conditions.

Many substances are used as adsorbents [11,12]; however, using metal oxides such as aluminum oxide (Al_2O_3), zinc oxide (ZnO), magnetic iron oxide (Fe_3O_4), and zirconium oxide (ZrO_2) as adsorbents is promising for removing different organic and inorganic pollutants from water because they have several advantages such as the simplicity of operation and the cost effectiveness [13–15]. Among these oxides, ZrO_2 is a preferred choice for removing different contaminants from water owing to its non-toxicity, high specific surface area, and ease of synthesis. The presence of both surface acidic and basic centers also makes it a promising adsorbent for the removal of many kinds of pollutants, and its adsorption capability can be modified significantly when combined with other substances [16,17].

ZrO_2 was synthesized by different physicochemical methods [18–21]. Using non-toxic and environmentally benign reagents and solvents are a key issue in green synthesis routes. In this context, using plant extracts in particular has many advantages since this reduces the number of hazardous chemicals utilized in the synthesis processes of such adsorbents [22–26]. In addition, phytochemicals in the plant extract act as reducing, precipitating, and capping agents and thus play an important role in controlling particle size, shape, phase stability, and other characteristics of nanomaterials [27,28].

Peppermint (*Menthapiperita* L.) is a medicinal herb used as flavoring agent in pharmaceutics and cosmetics, etc. In addition, it is a natural hybrid herb belonging to the *Lamiaceae* family, its major components being menthol, menthone, neomenthol, and isomenthone [29,30].

Trace levels of some heavy metals, such as cobalt, are important for the structure of various biological species [31]. However, a high concentration of these heavy metals is toxic [32–34] principally due to its accumulation in biological systems. As some heavy metals are essential in the industries of pigments, electronics, paints, and metallurgy, the discharges from these industries contain considerable amounts of these persistent and non-biodegradable species that result in serious environmental pollution [35]. The adsorption of Co^{2+} by different types of adsorbents was reported [36,37]. Some of these methods reported that the efficiency of adsorption is dependent on Co^{2+} concentration—being high at low Co^{2+} concentrations but decreasing significantly at high Co^{2+} concentrations [37].

To the best of our knowledge, there is no work on using peppermint extract as a precipitating and capping agent in the literature for the synthesis of ZrO_2. Thus, the aim of this study is to green synthesize ZrO_2NPs using an aqueous peppermint extract as the precipitant and stabilizing agent, and to investigate its characteristics and efficiency as an adsorbent for Co^{2+} removal from water.

2. Results and Discussion

2.1. XRD Analysis

The XRD patterns of ZrO_2NPs570 and ZrO_2NPs700 are shown in Figure 1. These patterns show diffraction peaks at 2 theta values corresponding to the (111), (200), (220), (311), (400), (331), and (422) planes of cubic ZrO_2 Fm-3m (225) (COD 9009051) [38,39]. It is also clear from Figure 1 that the peak intensities increase little with the increasing calcination temperature from 570 to 700 °C. On the other hand, the broadening of the XRD peaks indicates that the crystallite sizes of the samples are in the nanoscale [40]. The crystallite sizes of the ZrO_2NPs estimated using the Scherrer equation [41] from peaks 111, 220, and 311 averaged 6.27 and 7.26 nm for ZrO_2NPs570 and ZrO_2NPs700, respectively, as can be seen in Table 1.

Table 1. Crystallite size, BET surface area, and pore dimensions of ZrO_2NPs570 and ZrO_2NPs700.

	$ZrO_2$570	**$ZrO_2$700**
Average crystallite size, nm (XRD)	6.27	7.26
Average particle size, nm (TEM)	7.5	8.1
Surface area, m^2/g (BET)	94.805	62.384
Surface area, m^2/g (BJH)	80.329	61.222
Mean pore diameter, nm (BET)	3.922	7.588
Mean pore diameter, nm (BJH)	3.92	7.32
Total pore volume, cm^3/g (BET)	0.09296	0.1183
Pore volume, cm^3/g (NLDFT)	0.0698	0.06098
Pore volume, cm^3/g (BJH)	0.08513	0.1164

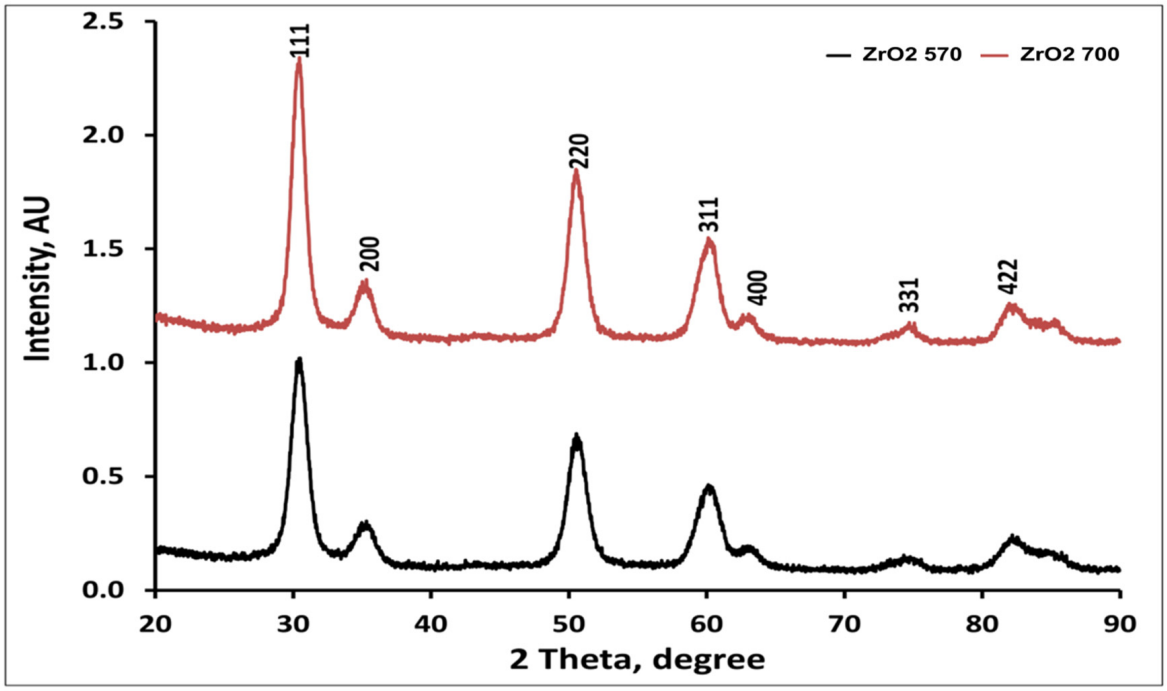

Figure 1. XRD patterns of ZrO_2NPs570 and ZrO_2NPs700.

2.2. Transmission Electron Microscopy

TEM provides valuable information about the particle size and shape. Therefore, the changes in particle size and shape accompanying calcination at different temperatures can be examined. The TEM images of the two $ZrO_2$570 and $ZrO_2$700 samples are given in Figure 2a,b and their particle size distributions are in Figure 2c,d, respectively. It is clear that the particles of the two samples are nearly spherical, with diameters in the range of 7–8 nm, which are comparable to the crystallite sizes calculated from the XRD data. This small size of the nanoparticles may be attributed to the capping effect of the phytochemicals in PAE which hinders growth of nanoparticles. It is also evident that neither the shape nor the size of the particles is largely affected by increasing the calcination temperature from 570 to 700 °C.

2.3. BET Surface Area

The nitrogen sorption isotherms and the corresponding pore distribution of ZrO_2NPs570 and ZrO_2NPs700 are presented in Figure 3a–d. The respective specific surface areas were measured to be 94.805 and 62.384 $m^2 \cdot g^{-1}$ for ZrO_2NPs570 and ZrO_2NPs700 as can be seen in Table 1. According to the values in this table, the calculated pore diameter doubles due to the increasing calcination temperature, while the pore volume is little affected. This may be due to the pores becoming less deep for the sample calcined at the higher temperature. The N_2 adsorption/desorption isotherms in Figure 3, and the values of pore diameter calculated in Table 1, suggest that ZrO_2 synthesized by this method is mesoporous and the isotherms with their hysteresis loops can be classified as type IV [42].

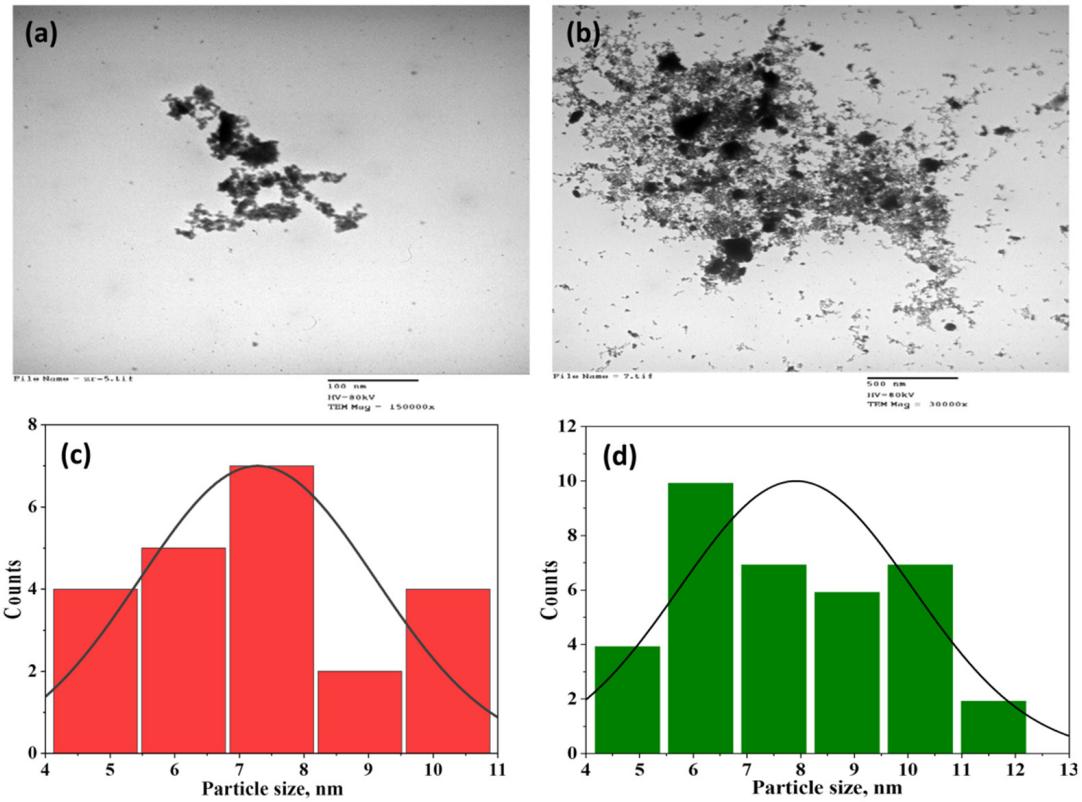

Figure 2. TEM images of (**a**) ZrO_2NPs570 (scale bar: 100 nm), (**b**) ZrO_2NPs700 (scale bar: 500 nm), and their respective particle-size distributions (**c**,**d**).

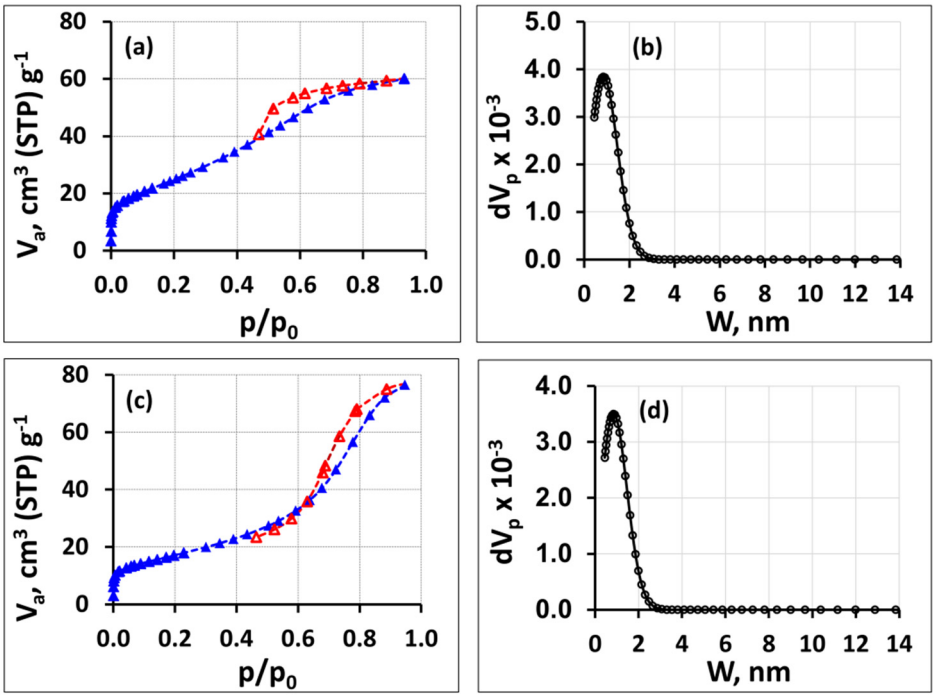

Figure 3. The nitrogen adsorption/desorption isotherms and the corresponding pore size distribution of (**a**,**b**) ZrO_2NPs570 and (**c**,**d**) ZrO_2NPs700. (Blue lines are adsorption and red lines are desorption in (**a**,**c**).

2.4. Mechanism of ZrO_2NPs Green Synthesis

The main phytochemicals in peppermint are menthol and menthone [29,30]. The possible mechanism for ZrO_2NPs formation is shown in Scheme 1. A complex is formed between Zr^{4+} ions and menthol molecules in aqueous medium. The complex is capped by other organic molecules, terminating further growth of the particles. Calcination of the complex then results in the formation of ZrO_2NPs via oxidation by oxygen in air [27,28].

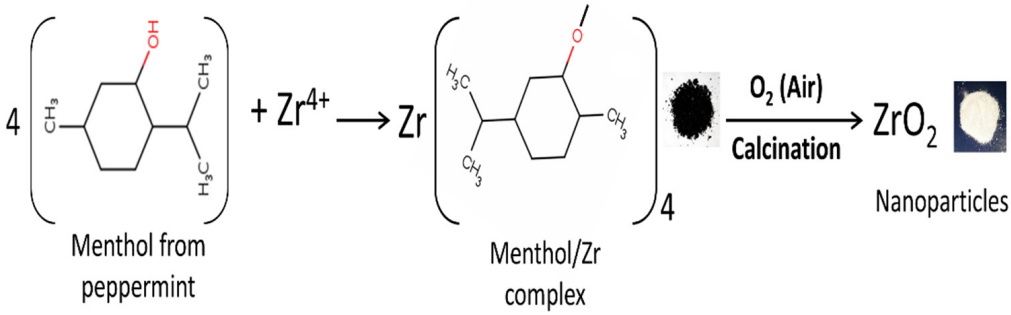

Scheme 1. Mechanism for green synthesis of ZrO_2NPs using peppermint.

2.5. Adsorption of Co^{2+} by ZrO_2NPs and Optimization of Adsorption Parameters

Preliminary experiments on cobalt ion adsorption by the synthesized ZrO_2NPs showed that ZrO_2NPs570 had a significantly higher adsorption efficiency than ZrO_2NPs700. ZrO_2NPs570 was, therefore, used for further adsorption studies.

2.5.1. Effect of pH

The adsorption phenomenon involves concentration of the adsorbate molecules onto the adsorbent surface. The electrostatic attraction between the surface and the adsorbate species is a major mechanism by which adsorption occurs. The nature and magnitude of the adsorbent surface charge, and also the charge on the adsorbate molecules, are affected by the pH value of the medium and, as a result, the adsorption process is pH dependent [43]. To determine the optimum pH for the uptake of Co^{2+} by the ZrO_2 surface, the pH value of the Co^{2+} solution was adjusted at 3, 5, 6.5 and 7.5. pH values equal to or higher than 8.5, resulting in the precipitation of Co^{2+}.

In this study, 6 $g \cdot L^{-1}$ of the adsorbent was used with 50 mL of 150 ppm Co^{2+} aqueous solution. The pH values were adjusted by the addition of NaOH or HCl (0.1 M each) at 25 °C and the adsorption lasted for 30 min. It is clear from Figure 4a that the adsorption of cobalt (R% and q_e) increases with increasing pH. The R% reaches about 45% at pH 7.5. To understand this effect of the pH on the efficiency of ZrO_2NPs as an adsorbent, the value of the point of zero charge (PZC) of the adsorbent should be considered [44]. The PZC value of ZrO_2 used in this study was determined to be 6.0 using a simple method [45] and is shown Figure 4b. The negatively charged surface of ZrO_2 at the higher pH values (6.5 and 7.5) favors the adsorption of the positively charged Co^{2+}. Protonation of the active surface sites at pH values lower than the PZC decreases the tendency of interaction of the positively charged cobalt with the surface [46].

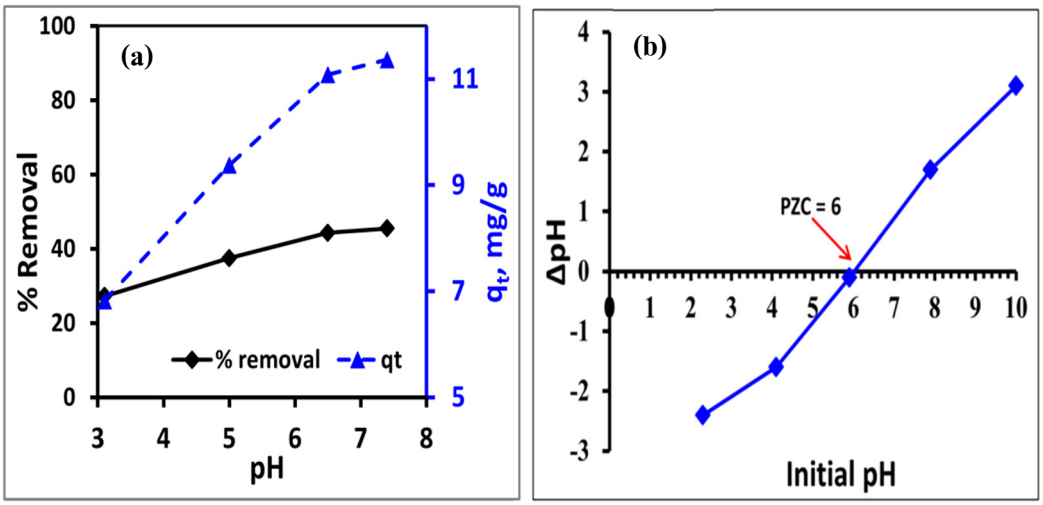

Figure 4. (**a**) Effect of pH on adsorption of Co^{2+} by ZrO_2NPs (ZrO_2 mass: 0.3 g, vol: 50 mL, Co^{2+} conc.: 150 ppm, time: 30 min, Temp.: 25 °C) and (**b**) The point of zero charge of ZrO_2NPs570.

2.5.2. Effect of Contact Time

It is important to determine the equilibrium contact time under the experimental conditions used. Equilibrium concentration values are required for estimation of different adsorption parameters and also for consideration of the adsorption process for application on the industrial scale. Contact time was investigated with different adsorbate concentrations, using adsorbent masses of 6 $g \cdot L^{-1}$. In all cases, as indicated in Figure 5, the incremental increase in the R% decreases gradually with time where the lines tend to flatten down with the progress of adsorption. The initial relatively fast uptake of cobalt is accounted for by the availability of surface adsorption sites in the initial adsorption stage. At longer contact times, the tendency of surface sites to bind Co^{2+} decreases due to the depletion of cobalt concentration with time, and also due to the development of surface electrostatic repulsion between adsorbed cobalt ions for a contact time of about 30 min, where equilibrium is assumed to be reached under the experimental conditions. This behavior is frequently encountered in adsorption studies [47,48]. Figure 6, on the other hand, indicates that q_t increases with increasing time until equilibrium is reached, as is expected.

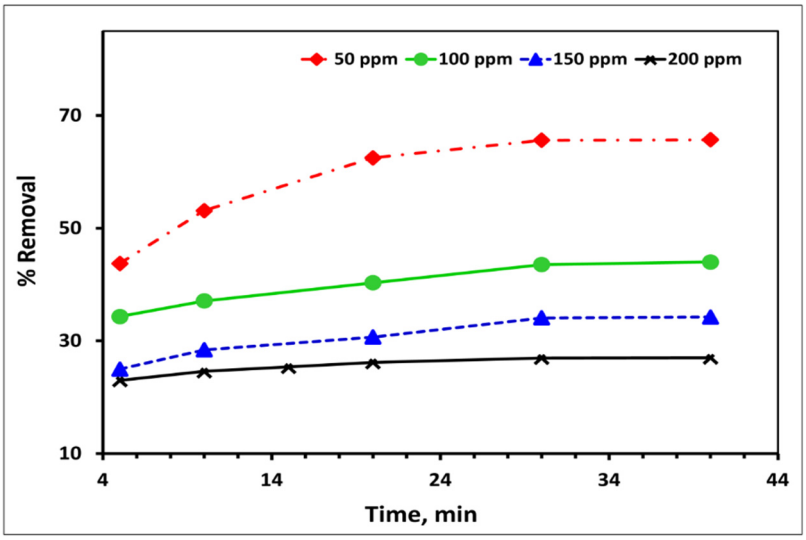

Figure 5. Effect of contact time on the % removal of cobalt by ZrO_2NPs570 (λ = 667, Volume: 50 mL, Conc.: 50–200 ppm, pH: 6.5, ZrO_2 mass: 0.3 g).

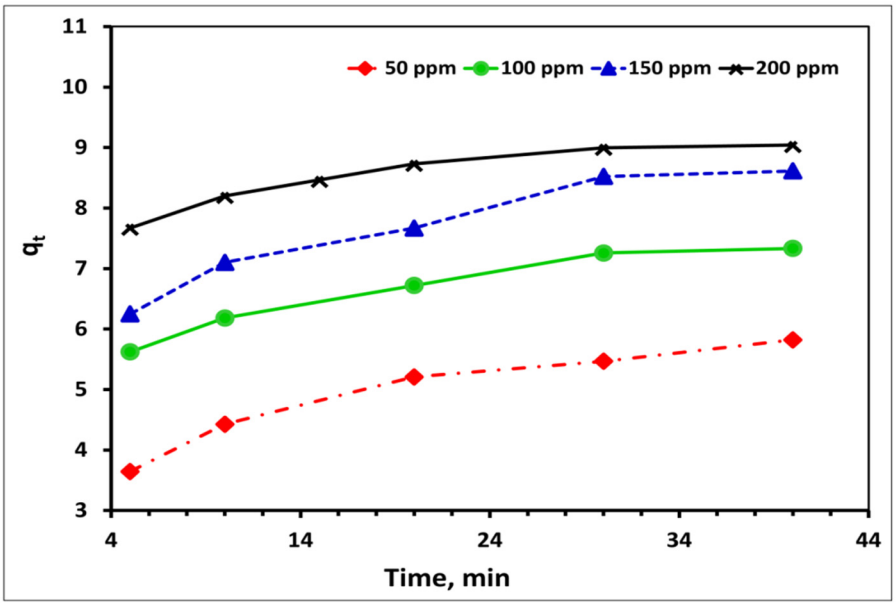

Figure 6. Effect of contact time on q_t during the removal of cobalt by ZrO_2NPs570 (λ = 667, Volume: 50 mL, Conc.: 50–200 ppm, pH: 6.5, ZrO_2 mass: 0.3 g).

2.5.3. Effect of Adsorbent Mass

In adsorption studies, the achievement of the maximum degree of adsorption is required. Accordingly, an important factor to study is the optimum mass of the adsorbent under experimental conditions. The effect of the amount of adsorbent on its efficiency for the removal of Co^{2+} was studied using ZrO_2NPs masses in the range 2–10 g·L^{-1}. As can be seen from Figure 7a, the Co^{2+} % removal increases with increasing ZrO_2NPs mass. This direct proportionality between adsorbent mass and %R at a fixed adsorbate concentration of 100 ppm can be explained by the availability of adsorption sites responsible for the uptake of Co^{2+} with increasing ZrO_2 mass [49]. On the other hand, the decrease in the equilibrium adsorption capacity from about 6.4 mg·g^{-1} at the beginning to about 5.2 mg·g^{-1} at the end is mainly due to the fact that an increasing adsorbent mass for a fixed Co^{2+} concentration results in a larger degree of unsaturation of adsorption sites.

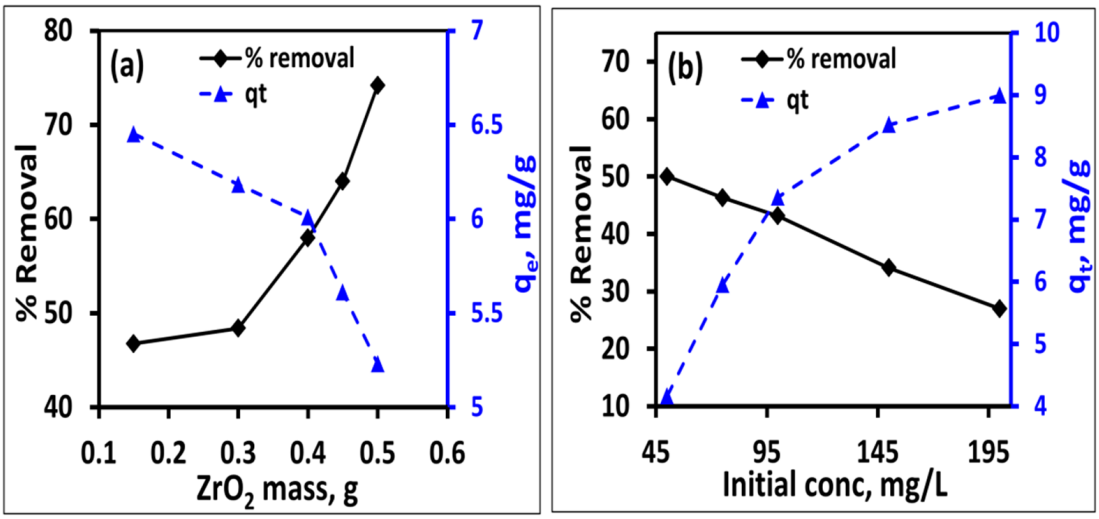

Figure 7. Effect of (**a**) ZrO_2NPs mass (λ = 667, time: 30 min, volume: 50 mL, Co^{2+} conc.: 100 ppm, pH: 6.5) and (**b**) initial Co^{2+} concentration on its % removal (λ = 667, time: 30 min, volume: 50 mL, ZrO_2 mass: 0.3 g, pH: 6.5).

2.5.4. Effect of Initial Co^{2+} Concentration

The effect of initial Co^{2+} concentration on its equilibrium adsorption % removal by ZrO_2NPs was investigated at different initial Co^{2+} concentrations in the range of 50–200 mg·L^{-1} at a fixed adsorbent mass of 6 g·L^{-1}. The results of this study are summarized in Figure 7b. It is clear that the % removal of Co^{2+} by ZrO_2NPs decreases with the increase in initial cobalt concentration. The percent removal of Co^{2+} decreases from 50% to 28.6% when the initial Co^{2+} concentration is increased from 50 to 200 mg·L^{-1} at a fixed adsorbent mass. However, the amount of Co^{2+} adsorbed by the fixed amount of adsorbent (q_t) nearly doubles (from about 4 to about 9 mg·g^{-1}) when the cobalt concentration is increased in the same range (from 50 to 200 mg·L^{-1}). An increase in the cobalt ion concentration is accompanied by an increase in the degree of interaction between Co^{2+} ions in the aqueous phase and surface of the adsorbent, according to the law of mass action. In addition, the increase in the amount of Co^{2+} adsorbed when the adsorbate concentration is increased can be explained by the fact that a high concentration of Co^{2+} creates a higher driving force for mass transfer between the adsorbent surface and adsorbate [50]. It is worth noting that the adsorption capacity value obtained in our experiments (~9 mg·g^{-1}) approximately equals a previously published value (9.43 mg·g^{-1}) in spite of the 10-fold higher temperature (250 °C) in the latter [51]. This may be attributed to the 4-fold higher surface area (94 m^2·g^{-1}) of the peppermint-mediated ZrO_2NPs than that of the chemically synthesized ZrO_2NPs (24 m^2·g^{-1}).

2.6. Adsorption Isotherms

Adsorption isotherms are theoretical relationships that correlate the adsorbate concentration in a medium to its equilibrium concentration onto the adsorbent surface at a certain constant temperature [52]. In addition, they play an important role in determining the adsorption capacities of the adsorbents. Furthermore, they give an insight into the degree of affinity of the adsorbent to the adsorbate species and the adsorption mechanism. The adsorption capacity was calculated from different equilibrium concentrations of the adsorbate and the experimental data obtained were fitted to Freundlich and Langmuir models at 298 K for initial Co^{2+} concentrations of 50, 100, 150, and 200 mg·L^{-1}. The linearized forms of the Langmuir and Freundlich isotherms are written in Equations (1) and (2), respectively [53,54]:

$$C_e/q_e = (1/K_L \cdot q_m) + (C_e/q_m) \quad (1)$$

$$\log q_e = (1/n) \log C_e + \log K_F \quad (2)$$

where q_e (mg·g^{-1}): equilibrium adsorption capacity, q_m (mg·g^{-1}): Langmuir maximum adsorption capacity, K_L (L·mg^{-1}): Langmuir constant, C_e (mg·L^{-1}): equilibrium adsorbate concentration in solution, K_F (mg·g^{-1})/(mg·L^{-1})$^{1/n}$: Freundlich adsorption capacity, and 1/n (dimensionless): Freundlich constant which provides adsorption intensity.

The Langmuir and Freundlich isotherms are presented at 298 K and an initial Co^{2+} concentration in the range 50–200 mg·L^{-1} in Figure 8a,c, respectively. The values of constants for each model were calculated to evaluate the adsorption characteristics and affinity of the adsorbent for Co^{2+} (Table 2). The results in Table 2 suggest that ZrO_2NPs are effective adsorbents for Co^{2+} uptake from the aqueous solution to form a monolayer of adsorbate on the surface of the adsorbent. According to the Langmuir model, the high value of K_L at room temperature indicates the strong affinity of Co^{2+} to the ZrO_2NPs surface and reflects the ability of the adsorbent to adsorb large amount of Co^{2+}. This agrees with previous studies that suggested the Langmuir adsorption isotherm for the adsorption of Co^{2+} by different adsorbents, including metal oxides [55–58]. The Langmuir equation also can be used to predict whether an adsorption system is favorable or unfavorable [53]. The adsorption intensity (R_L) can be defined by Equation (3):

$$R_L = 1/(1 + K_L C_o) \quad (3)$$

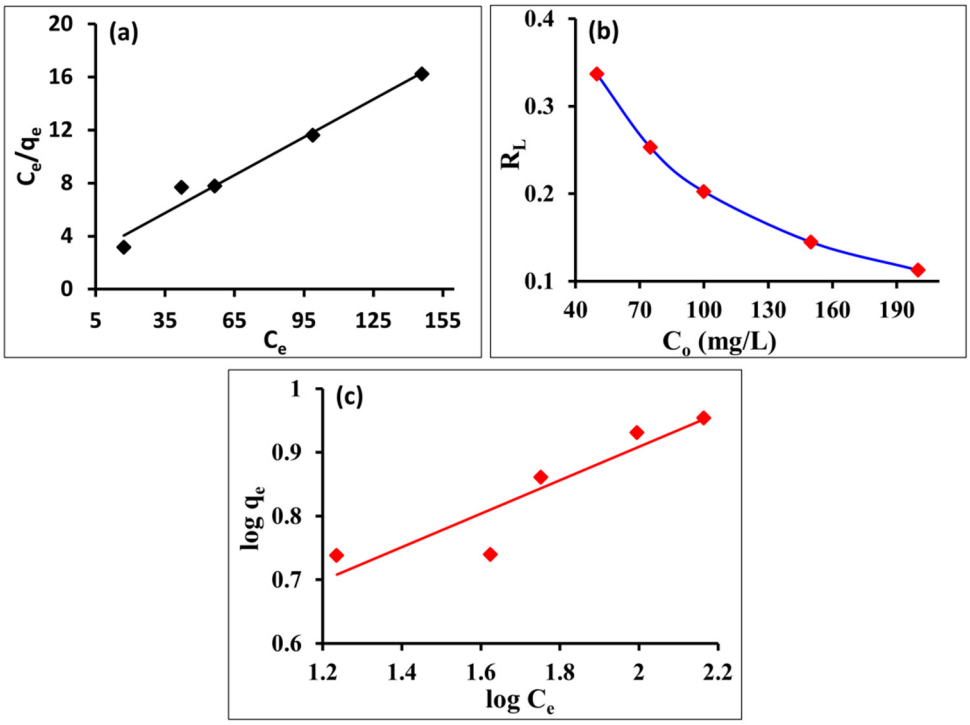

Figure 8. (**a**) Langmuir adsorption isotherm, (**b**) variation in R_L values and (**c**) Freundlich adsorption isotherm.

Table 2. The calculated adsorption isotherm parameters for Co^{2+} adsorption by ZrO_2.

T, K	Langmuir			Freundlich		
	q_m	K_L	R^2	n	K_F	R^2
298	8.995	0.039	0.973	3.810	2.420	0.840

The value of R_L indicates the favorability of the adsorption isotherm; irreversible ($R_L = 0$), favorable ($0 < R_L < 1$), linear ($R_L = 1$), or unfavorable ($R_L > 1$) [53]. The variation in adsorption intensity R_L with the initial concentration of the solution is presented in Figure 8b. The calculated R_L values are 0.337, 0.253, 0.202, 0.145, and 0.113 for the respective Co^{2+} initial concentrations of 50, 75, 100, 150, and 200 mg·L^{-1}. These values indicate a favorable and efficient adsorption process across the entire concentration range.

On the other hand, the empirical equation of the Freundlich model can be used to describe adsorption from a solution [53]. The linear equation for this model allows calculation of the values of the Freundlich isotherm constants (K_f and n). The high values of these constants show an easy uptake and good adsorption process of adsorbate from aqueous solutions, and also high adsorptive capacities at the studied conditions. The values of the Freundlich isotherm constants n and K_f for the adsorption of Co^{2+} by ZrO_2 are given in Table 2. Comparing the correlation coefficients, the R^2 values of both isotherms indicate that the results are best fitted by the Langmuir model.

2.7. Kinetics of the Adsorption of Co^{2+} onto ZrO_2NPs

Investigation of adsorption kinetics provides valuable information about the mechanism of the adsorption process. The kinetics of adsorbate uptake by the adsorbent was described by various models [59,60]. Of these, the pseudo-first order, pseudo-second order, the Elovich, and the intraparticle diffusion models were used in this study to test the experimental data. The respective linear equations for these four models are shown in Equations (4)–(7) [59,60].

$$\log (q_e - q_t) = \log q_e - (k_1/2.303)\, t \quad (4)$$

$$q_t = (1/k_2 q_e^2) + (1/q_e)\, t \quad (5)$$

$$q_t = (1/\beta) \ln \alpha\beta + (1/\beta) \ln t \quad (6)$$

$$q_t = k_i\, t^{0.5} + C \quad (7)$$

where q_t ($mg{\cdot}g^{-1}$): amount of adsorbate adsorbed at time t, k_1 (min^{-1}): pseudo-first order rate constant, k_2 ($g{\cdot}mg^{-1}{\cdot}min^{-1}$): pseudo-second order rate constant, α ($mg{\cdot}g^{-1}{\cdot}min^{-1}$): the initial adsorption rate, β ($g{\cdot}mg^{-1}$): parameter related to the extent of surface coverage and activation energy of the Elovich equation, k_i ($mg{\cdot}g^{-1}{\cdot}min^{-0.5}$): the intraparticle diffusion rate constant, and C: the width of the boundary layer.

Figure 9a–d presents the different models. The values of R^2 as well as the constants of the models are summarized in Table 3. As can be seen from this table, the obtained results are fitted well by the pseudo-second order model. This suggests that the uptake of Co^{2+} is a chemisorption process involving a physicochemical interaction between the Co^{2+} and the ZrO_2 surface.

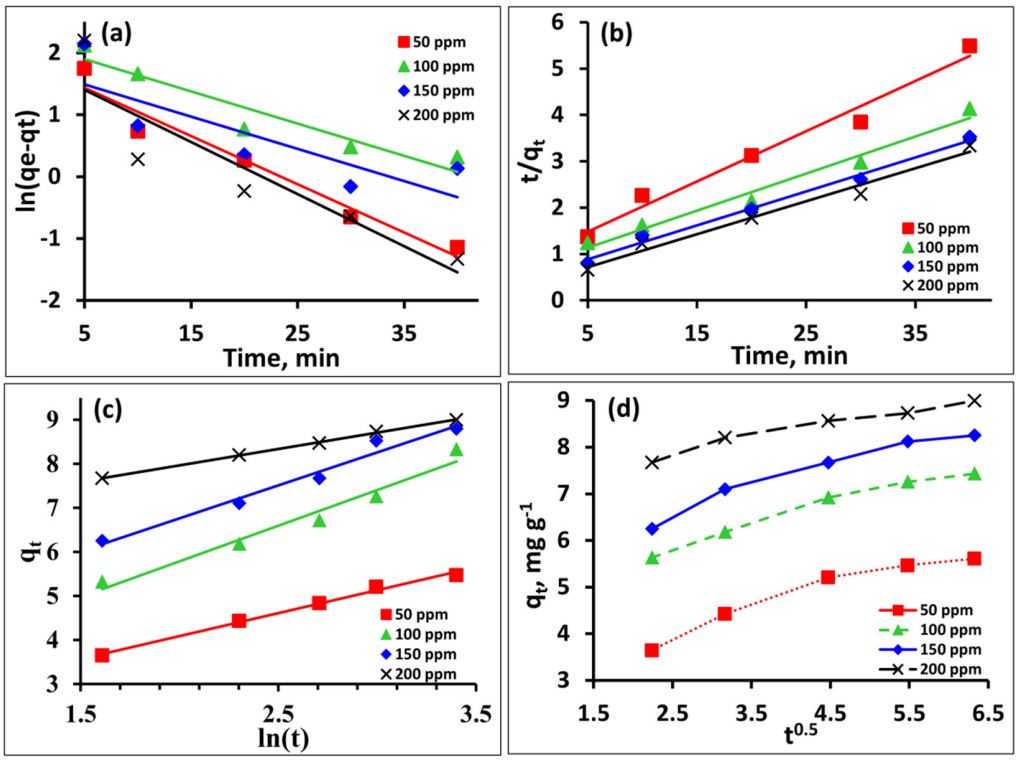

Figure 9. (**a**) Pseudo 1st order, (**b**) Pseudo 2nd order, (**c**) Elovich, and (**d**) Intraparticle diffusion models (50 mL, 50 ppm Co^{2+}, 0.3 g ZrO_2, time 30 min, temp 25 °C).

Table 3. Calculated kinetic model parameters for Co adsorption by ZrO_2.

C_0	Pseudo 1st Order			Pseudo 2nd Order			Elovich			$q_e$exp
	K_1	$q_e$calc	R^2	K_2	$q_e$calc	R^2	β	α	R^2	
50	0.078	6.207	0.955	0.0125	9.225	0.976	0.9613	1.749	0.993	5.469
100	0.052	8.669	0.901	0.009	12.500	0.977	0.617	2.316	0.965	7.258
150	0.052	5.744	0.676	0.010	13.643	0.989	0.668	2.048	0.974	8.523
200	0.084	6.187	0.818	0.0141	14.045	0.980	1.348	0.832	0.999	8.995

The Elovich equation posits that the active sites on the solid surface are diverse in character so they exhibit varied properties for chemisorption activation energies [61]. A linear characteristic is revealed by the values of (R^2) calculated from Figure 9c. Table 3 presents the α and β coefficients. In the Elovich model, α is proportional to the rate of change in chemisorption (initial adsorption rate), and β is related to surface amplification (desorption constant). High values of α and β indicate the rapid rate of chemisorption and the increase in the available adsorption surface for Co^{2+} [61]. Figure 9d shows the effect of intraparticle diffusion on adsorption. Fluid flow, film diffusion, and the plateau region are all represented by the three portions of this curve. The straight lines do not pass through the origin under the conditions tested, indicating that intraparticle diffusion is not the determining factor in the sorption process.

3. Materials and Methods

3.1. Synthesis of ZrO_2NPs

About 100 g of fresh green peppermint (whole plant) was washed with tap water, rinsed with distilled water (DW), dried in air for 48 h, cut into small pieces and then impregnated in DW for 24 h. The peppermint aqueous extract (PAE) was collected by filtration and was kept in refrigerator. Fifteen grams of zirconium oxychloride were dissolved in about 50 mL distilled water in a 500 mL Pyrex glass beaker. To this solution, the PAE (about 200 mL) was added dropwise while the mixture was subjected to continuous stirring. A pale brown precipitate was formed and was magnetically stirred for 2 h, filtered off, washed with DW several times, dried in air for 24 h, and then dried in an oven at 100 °C for 5 h to form a black solid [27], as shown in Scheme 2. The latter solid was carefully milled and calcined, in air, for 3 h at 570 and 700 °C to form ZrO_2NPs570 and ZrO_2NPs700, respectively.

3.2. Characterization

The phase compositions of the samples were determined using a powder X-ray diffractometer (X'Pert3 Powder, PAN Anlytical, Almelo, The Netherlands) operating at 40 KV and 30 mA using Cu-K_α = 1.54056 Å as a radiation source and a nickel filter. The crystallite size of different samples was calculated from the XRD data using the Scherrer equation: $D = K\lambda/\beta\cos\theta$, where D is the average crystallite size (nm), K is the full width at half maximum, θ is the Bragg angle, β is the shape factor, and λ is the wavelength = 1.54056 Å. A BEL SORP-MAX analyzer (Microtrac BEL, Osaka, Japan) was used to determine the adsorbent specific surface areas. A UV-vis spectrophotometer (PG Instruments, model T80, Leicestershire, UK) was used to measure the concentrations of Co^{2+} using quartz cells with a 1 cm path length. Transmission electron microscope (TEM) images were taken using a JEM-1010 transmission electron microscope operating at 70 KV and 58 μA. A portion of the sample was dispersed in absolute ethanol, sonicated, and a drop of the resulting suspension was taken on a carbon grid (200 mesh). Before being admitted to the microscope, the grid was left in air to evaporate the ethanol.

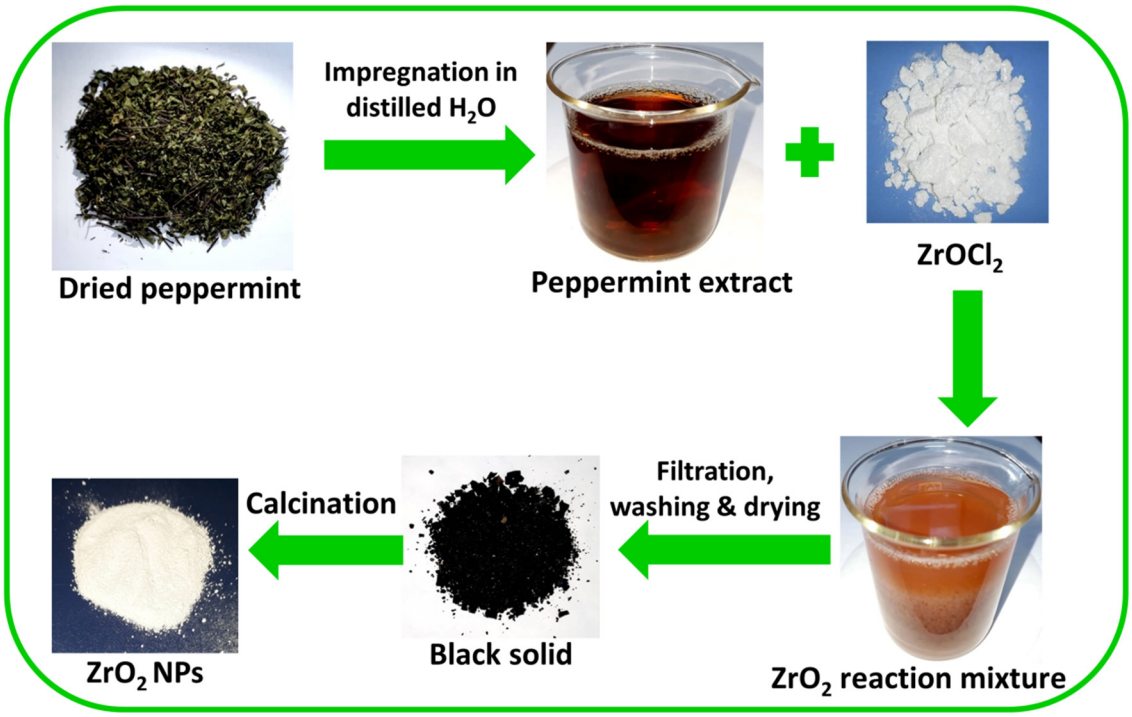

Scheme 2. Green synthesis of ZrO_2NPs from peppermint.

3.3. Adsorption Experiments

The adsorption experiments were performed in clean reagent bottles at room temperature. In these experiments, ZrO_2NPs were dispersed in a specific volume of Co^{2+} solution of known concentration, and the mixture was continuously agitated using a mechanical shaker at room temperature (25 ± 1 °C). The effects of different parameters influencing adsorption such as pH, initial Co^{2+} concentration, ZrO_2NPs mass, and contact time were studied. Adsorption conditions were optimized by changing one adsorption parameter while keeping the other parameters fixed [62]. After suitable treatment times, the adsorbents were separated from the treated solutions by centrifugation and the remaining Co^{2+} concentration in the solutions was determined by UV-vis spectroscopy [63]. The concentration of adsorbed Co^{2+} was calculated from the difference between the initial and final concentrations (C_o and C_f, respectively) of Co^{2+}. The removal percentage (R%) and the adsorption capacity (q_t) were estimated using the following Equations (8) and (9), respectively:

$$R\% = [(C_o - C_f)/C_o] \times 100 \quad (8)$$

$$q_t = [(C_o - C_f) \times V]/W \quad (9)$$

In Equation (2), V is the volume of the treated solution in liters and W is the weight of ZrO_2NPs utilized in the experiment in grams.

4. Conclusions

Peppermint-mediated green synthesis of ZrO_2NPs was described in this paper. The oxides calcined at 570 and 700 °C, $ZrO_2$570 and $ZrO_2$700, were characterized and used as adsorbents for the removal of cobalt ions from water. Different parameters affecting adsorption (pH, initial adsorbate concentration, adsorbent mass, and agitation time) were studied. Results show that ZrO_2NPs samples are mesoporous and can be used efficiently for the removal of cobalt from water. The adsorption follows a pseudo-second order kinetics and can be explained by the Langmuir adsorption isotherm.

Author Contributions: I.M.A.H.: conceptualization, methodology, preparation, investigation, writing—original draft; H.S.E.-D.: validation, writing—review and editing; A.A.A.: conceptualization, methodology, preparation, investigation, writing—original draft. All authors have read and agreed to the published version of the manuscript.

Funding: No funds were received for this study.

Institutional Review Board Statement: Not applicable.

Informed Consent Statement: Not applicable.

Data Availability Statement: The data presented in this study are available on request from the corresponding author.

Conflicts of Interest: The authors declare no conflict of interest.

References

1. Trejo-Arroyo, D.L.; Acosta, K.E.; Cruz, J.C.; Valenzuela-Muñiz, A.M.; Vega-Azamar, R.E.; Jiménez, L.F. Influence of ZrO_2 Nanoparticles on the Microstructural Development of Cement Mortars with Limestone Aggregates. *Appl. Sci.* **2019**, *9*, 598. [CrossRef]
2. Matt, S.B.; Shivanna, M.; Manjunath, S.; Siddalinganahalli, M.; Siddalingappa, D.M. Electrochemical Detection of Serotonin Using t-ZrO_2 Nanoparticles Modified Carbon Paste Electrode. *J. Electrochem. Soc.* **2020**, *167*, 155512. [CrossRef]
3. Mok, Z.H.; Proctor, G.; Thanou, M. Emerging nanomaterials for dental treatments. Emerg. *Top. Life Sci.* **2020**, *4*, 613–625.
4. Khan, M.; Shaik, M.R.; Khan, S.T.; Adil, S.F.; Kuniyil, M.; Khan, M.; Al-Warthan, A.A.; Siddiqui, M.R.H.; Tahir, M.N. Enhanced Antimicrobial Activity of Biofunctionalized Zirconia Nanoparticles. *ACS Omega* **2020**, *5*, 1987–1996. [CrossRef]
5. Ashiq, M.N.; Aman, A.; Alshahrani, T.; Iqbal, M.F.; Razzaq, A.; Najam-Ul-Haq, M.; Shah, A.; Nisar, J.; Tyagi, D.; Ehsan, M.F. Enhanced electrochemical properties of silvercoated zirconia nanoparticles for supercapacitor application. *J. Taibah Univ. Sci.* **2021**, *15*, 10–16. [CrossRef]
6. Shelke, G.B.; Patil, D.R. Gas Sensing Performance of Pure and Modified Nanostructured Screen Printed Zirconia Thick Films. *Int. J. Eng. Res. Technol.* **2019**, *8*, 198–202.
7. Chikere, C.O.; Faisal, N.H.; Kong-Thoo-Lin, P.; Fernandez, C. Interaction between Amorphous Zirconia Nanoparticles and Graphite: Electrochemical Applications for Gallic Acid Sensing Using Carbon Paste Electrodes in Wine. *Nanomater* **2020**, *10*, 537. [CrossRef]
8. Annu, A.; Sivasankari, C.; Krupasankar, U. Synthesis and characterization of ZrO_2 nanoparticle by leaf extract bioreduction process for its biological studies. *Mater. Today Proc.* **2020**, *33*, 5317–5323. [CrossRef]
9. Demirbas, E. Adsorption of Cobalt(II) Ions from Aqueous Solution onto Activated Carbon Prepared from Hazelnut Shells. *Adsor. Sci. Technol.* **2003**, *21*, 951–963. [CrossRef]
10. Patel, H. Charcoal as an adsorbent for textile wastewater Treatment. *Sep. Sci. Technol.* **2018**, *53*, 2797–2812. [CrossRef]
11. Rajendran, S.; Priya, A.K.; Kumar, P.S.; Hoang, T.K.A.; Sekar, K.; Chong, K.Y.; Khoo, K.S.; Ng, H.S.; Show, P.L. A critical and recent developments on adsorption technique for removal of heavy metals from wastewater-A review. *Chemosphere* **2022**, *303*, 135146. [CrossRef]
12. Zou, W.; Bai, H.; Zhao, L.; Li, K.; Han, R. Characterization and properties of zeolite as adsorbent for removal of uranium (VI) from solution in fixed bed column. *J. Nucl. Chem.* **2011**, *288*, 779–788. [CrossRef]
13. Gua, M.; Haoa, L.; Wang, Y.; Li, X.; Chen, Y.; Li, W.; Jiang, L. The selective heavy metal ions adsorption of zinc oxide nanoparticles from dental wastewater. *Chem. Phys.* **2020**, *534*, 110750. [CrossRef]
14. Roto, R. Surface Modification of Fe_3O_4 as Magnetic Adsorbents for Recovery of Precious Metals. In *Advanced Surface Engineering Research*; Chowdhury, M.A., Ed.; Intechopen: London, UK, 2018; pp. 127–145. [CrossRef]
15. Viana da Silva, A.F.; Fagundes, A.P.; Macuvele, D.L.P.; Urano de Carvalho, E.F.; Durazzo, M.; Padoin, N.; Soares, C.; Riella, H.G. Green synthesis of zirconia nanoparticles based on *Eucleanatalensis* plant extract: Optimization of reaction conditions and evaluation of adsorptive properties. *Colloids Surf. A Physicochem. Eng. Asp.* **2019**, *583*, 123915. [CrossRef]
16. Navı´o, J.A.; Hidalgo, M.C.; Colo´n, G.; Botta, S.G.; Litter, M.I. Preparation and Physicochemical Properties of ZrO_2 and Fe/ZrO_2 Prepared by a Sol-Gel Technique. *Langmuir* **2001**, *17*, 202–210. [CrossRef]
17. Gurushantha, K.; Anantharaju, K.S.; Nagabhushana, H.; Sharma, S.C.; Vidya, Y.S.; Shivakumara, C.; Nagaswarupa, H.P.; Prashantha, S.C.; Anilkumar, M.R. Facile green fabrication of iron-doped cubic ZrO_2 nanoparticles by Phyllanthusacidus: Structural, photocatalytic and photoluminescent properties. *J. Mol. Catal. A Chem.* **2015**, *397*, 36–47. [CrossRef]
18. Behbahani, A.; Rowshanzamir, S.; Esmaeilifar, A. Hydrothermal synthesis of zirconia nanoparticles from commercial zirconia. *Procedia Eng.* **2012**, *42*, 908–917. [CrossRef]
19. Singh, A.K.; Nakate, U.T. Microwave Synthesis, Characterization and Photoluminiscence Properties of Nanocrystalline Zirconia. *Sci. World J.* **2014**, *2014*, 349457. [CrossRef]
20. Dang, Y.Y.; Bhuiyan, M.S.; Paranthaman, M.P. Zirconium oxide nanostructures prepared by anodic oxidation. *U.S. Dep. Energy J. Undergrad. Res.* **2008**, *8*, 48–53.

21. Zhu, H.Y.; Liu, B.; Shen, M.M.; Kong, Y.; Hong, X.; Hu, Y.H.; Ding, W.P.; Dong, L.; Chen, Y. Effect of maltose for the crystallization of tetragonal zirconia. *Mater. Lett.* **2004**, *58*, 3107–3110. [CrossRef]
22. Nimare, P.; Koser, A.A. Biological Synthesis of ZrO_2 Nanoparticle Using Azadirachta Indica Leaf Extract. *Int. Res. J. Eng. Technol.* **2016**, *3*, 1910–1912.
23. Al-Zaqri, N.; Muthuvel, A.; Jothibas, M.; Alsalme, A.; Alharthi, F.A.; Mohana, V. Biosynthesis of zirconium oxide nanoparticles using Wrightiatinctoria leaf extract: Characterization, photocatalytic degradation and antibacterial activities. *Inorg. Chem. Commun.* **2021**, *127*, 108507. [CrossRef]
24. Shinde, H.M.; Bhosale1, T.T.; Gavade, N.L.; Babar, S.B.; Kamble, R.J.; Shirke, B.S.; Garadkar, K.M. Biosynthesis of ZrO_2 nanoparticles from Ficusbenghalensis leaf extract for photocatalytic activity. *J. Mater. Sci. Mater. Electron.* **2018**, *29*, 14055–14064.
25. Majedi, A.; Abbasi, A.; Davar, F. Green synthesis of zirconia nanoparticles using the modified Pechini method and characterization of its optical and electrical Properties. *J. Sol-Gel Sci. Technol.* **2016**, *77*, 542–552. [CrossRef]
26. Shanthi, S.; Tharani, S.S.N. Green Synthesis of Zirconium Dioxide (ZrO_2) Nano Particles Using Acalypha Indica Leaf Extract. *Int. J. Eng. Appl. Sci.* **2016**, *3*, 23–25.
27. Hasan, I.M.A.; Tawfik, A.R.; Assaf, F.H. GC/MS screening of buckthorn phytochemicals and their use to synthesize ZnO nanoparticles for photocatalytic degradation of malachite Green dye in water. *Water Sci. Technol.* **2021**, *85*, 666. [CrossRef]
28. Huang, Y.; Haw, C.; Zheng, Z.; Kang, J.; Zheng, J.; Wang, H. Biosynthesis of zinc oxide nanomaterials from plant extracts and future green prospects: A topical review. *Adv. Sustain. Syst.* **2021**, *5*, 2000266. [CrossRef]
29. Zhao, H.; Ren, S.; Yang, H.; Tang, S.; Guo, C.; Liu, M.; Tao, Q.; Ming, T.; Xu, H. Peppermint essential oil: Its phytochemistry, biological activity, pharmacological effect and application. *Biomedi. Pharmacother.* **2022**, *154*, 113559. [CrossRef]
30. Marwa, C.; Fikri-Benbrahim, K.; Ou-Yahia, D.; Farah, A. African peppermint (*Menthapiperita*) from Morocco: Chemical composition and antimicrobial properties of essential oil. *J. Adv. Pharm. Technol. Res.* **2017**, *8*, 86–90.
31. González-Montaña, J.R.; Escalera, F.; Alonso, A.J.; Lumillos, J.M.; Robles, R.; Alonso, M. Relationship between Vitamin B12 and Cobalt Metabolism in Domestic Ruminant: An Update. *Animal* **2020**, *10*, 1855. [CrossRef]
32. Jaiswal, A.K.; Kumar, R.; Thakur, A.; Pori, P.; Kumara, R.; Kanojia, R. Cobalt Toxicity/Poisoning with analytical aspects and its Manaagment. *Int. J. Med. Lab. Res.* **2019**, *4*, 29–36. [CrossRef]
33. Czarnek, K.; Terpiłowska, S.; Siwicki, A.K. Selected aspects of the action of cobalt ions in the human body. *Cent. Eur. J. Immunol.* **2015**, *40*, 236–242. [CrossRef] [PubMed]
34. Gómez-Arnaiz, S.; Tate, R.J.; Grant, M.H. Cobalt neurotoxicity: Transcriptional Effect of elevated cobalt blood levels in the rodent brain. *Toxics* **2022**, *10*, 59. [CrossRef] [PubMed]
35. Alloway, B.J.; Ayres, D.C. *Chemical Principles of Environmental Pollution*; Chapman and Hall: Oxford, UK, 1993.
36. Caramalau, C.; Bulgariu, L.; Macobeanu, M. Kinetic study of cobalt adsorption on peat activated by simple chemical treatment. *Envron. Eng. Manag. J.* **2009**, *8*, 1351–1358.
37. Caramalau, C.; Bulgariu, L.; Macobeanu, M. Adsorption Characteristics of Cobalt(II) ions from aqueous solution on Romanian peat moss. *Environ. Eng. Manag. J.* **2009**, *8*, 1089–1095.
38. Basahel, S.N.; Ali1, T.T.; Mokhtar, M.; Narasimharao, K. Influence of crystal structure of nanosized ZrO_2 on photocatalytic degradation of methyl orange. *Nanoscale Res. Lett.* **2015**, *10*, 73. [CrossRef]
39. Manivasakan, P.; Rajendran, V.; Rauta, P.R.; Sahu, B.B.; Panda, B.K. Synthesis of Monoclinic and Cubic ZrO_2 Nanoparticles from Zircon. *J. Am. Ceram. Soc.* **2011**, *94*, 1410–1420. [CrossRef]
40. Andrade, A.B.; Ferreira, N.S.; Valerio, M.E.G. Particle size effects on structural and optical properties of BaF_2 nanoparticles. *RSC Adv.* **2017**, *7*, 26839. [CrossRef]
41. Bokuniaeva, A.O.; Vorokh, A.S. Estimation of particle size using the Debye equation and the Scherrer formula for polyphasic TiO_2 powder. *J. Phys. Conf. Ser.* **2019**, *1410*, 012057. [CrossRef]
42. Thommes, M.; Kaneko, K.; Neimark, A.V.; Olivier, J.P.; Rodriguez-Reinoso, F.; Rouquerol, J.; Sing, K.S.W. Physisorption of gases, with special reference to the evaluation of surface area and pore size distribution (IUPAC technical report). *Pure. Appl. Chem.* **2015**, *87*, 1051–1069. [CrossRef]
43. Cruz-Lopes, L.P.; Macena, M.; Esteves, B.; Guiné, R.P.F. Ideal pH for the adsorption of metal ions Cr^{6+}, Ni^{2+}, Pb^{2+} in aqueous solution with different adsorbent materials. *Open Agric.* **2021**, *6*, 115–123. [CrossRef]
44. Kosmulski, M. The pH dependent surface charging and points of zero charge VIII. Update. *Adv. Colloid Interface Sci.* **2020**, *275*, 102064. [CrossRef] [PubMed]
45. Al-Maliky, E.A.; Gzar, H.A.; Al-Azawy, M.G. Determination of Point of Zero Charge (PZC) of Concrete Particles Adsorbents. *IOP Conf. Ser. Mater. Sci. Eng.* **2021**, *1184*, 012004. [CrossRef]
46. Abate, G.Y.; Alene, A.N.; Habte, A.T.; Addis, Y.A. Adsorptive removal of basic green dye from aqueous solution using humic acid modified magnetite nanoparticles: Kinetics, equilibrium and thermodynamic studies. *J. Polym. Environ.* **2021**, *29*, 967–984. [CrossRef]
47. Azman, A.; Ngadi, N.; Awg Zaini, D.K.; Jusoh, M.; Mohamad, Z.; Arsad, A. Effect of adsorption parameter on the removal of aspirin using tyre waste adsorbent. *Chem. Eng. Trans.* **2019**, *72*, 157–162.
48. Gulipalli, C.H.S.; Prasad, B.; Wasewar, K.L. Bach study, Equilibrium and kinetics of adsorption of selenium using rich husk ash (RHA). *J. Eng. Sci. Technol.* **2011**, *6*, 586–605.

49. Altintig, E.; Yenigun, M.; Sari, A.; Altundag, H.; Tuzen, M.; Saleh, T.A. Facile synthesis of zinc oxide nanoparticles loaded activated carbon as an eco-friendly adsorbent for ultra-removal of malachite green from water. *Environ. Technol. Innov.* **2021**, *21*, 101305. [CrossRef]
50. Al-Musawi, T.J.; Arghavan, S.M.A.; Allahyari, E.; Arghavan, F.S.; Othmani, A.; Nasseh, N. Adsorption of malachite green dye onto almond peel waste: A study focusing on application of the ANN approach for optimization of the effect of environmental parameters. *Biomass Convers. Biorefin.* **2022**, 1–13. [CrossRef]
51. Kim, Y.-H. Adsorption Characteristics of Cobalt on ZrO_2 and Al_2O_3 Adsorbents in High-Temperature Water. *Sep. Sci. Technol.* **2000**, *35*, 2327–2341. [CrossRef]
52. Barrow, G.M. *Physical Chemistry*, 5th ed.; McGrow-Hill: Singapore, 1988.
53. Tang, R.; Hong, W.; Srinivasakannan, C.; Liu, X.; Wang, X.; Duan, X. A novel mesoporous Fe-silica aerogel composite with phenomenal adsorption capacity for malachite green. *Sep. Purif. Technol.* **2022**, *281*, 119950. [CrossRef]
54. Wang, J.; Guo, X. Adsorption isotherm models: Classification, physical meaning, application and solving method. *Chemosphere* **2020**, *258*, 127279. [CrossRef] [PubMed]
55. Essaadaoui, Y.; Lebkiri, A.; Rifi, E.; Kadiri, L.; Ouass, A. Adsorption of cobalt from aqueous solutions onto Bark of Eucalyptus. Mediterranean. *J. Chem.* **2018**, *7*, 145–155.
56. Ramos, S.N.C.; Xavier, A.L.P.; Teodoro, F.S.; Gil, L.F.; Gurgel, L.V.A. Removal of cobalt(II), copper(II), and nickel(II) ions from aqueous solutions using phthalate-functionalized sugarcane bagasse: Mono-and multicomponent adsorption in batch mode. *Ind. Crops Prod.* **2016**, *79*, 116–130. [CrossRef]
57. Ketsela, G.; Animen, Z.; Talema, A. Adsorption of Lead (II), Cobalt (II) and Iron (II) From Aqueous Solution by Activated Carbon Prepared from White Lupine (GIBITO) HSUK. *J. Thermodyn. Catal.* **2020**, *11*, 203.
58. Rengaraj, S.; Moon, S. Kinetics of adsorption of Co(II) removal from water and wastewater by ion exchange resins. *Water Res.* **2002**, *36*, 1783–1793. [CrossRef]
59. Wanga, J.; Guo, X. Adsorption kinetic models: Physical meanings, applications, and solving methods. *J. Hazard. Mater.* **2020**, *390*, 122156. [CrossRef]
60. Wang, L.; Shi, C.; Wang, L.; Pan, L.; Zhang, X.; Zou, J. Rational design, synthesis, adsorption principles and applications of metal oxide adsorbents: A review. *Nanoscale* **2020**, *12*, 4790–4815. [CrossRef]
61. Mahadevan, H.; Nimina, P.V.M.; Krishnan, K.A. An environmental green approach for the effective removal of malachite green from estuarine waters using Pistaciavera L. shell-based active carbon. Sustain. *Water Resour. Manag.* **2022**, *8*, 38.
62. Hasan, I.M.A.; Tawfik, A.R.; Assaf, F.H. Biosynthesis of α-MoO_3 nanoparticles and its adsorption performance of cadmium from aqueous solutions. *Adv. Nat. Sci. Nanosci. Nanotechnol.* **2021**, *12*, 035007. [CrossRef]
63. Khan, M.I.; Kazmi, S.A. Spectrophotometric determination of cobalt(II). *J. Chem. Soc. Pak.* **1979**, *1*, 73–74.